

Nonsymmorphic symmetry-protected topological modes in plasmonic nanoribbon latticesYong-Liang Zhang,¹ Raymond P. H. Wu,¹ Anshuman Kumar,² Tieyan Si,³ and Kin Hung Fung^{1,*}¹*Department of Applied Physics, The Hong Kong Polytechnic University, Hong Kong, China*²*Department of Physics, Indian Institute of Technology Bombay, Powai, Mumbai 400076, Maharashtra, India*³*Academy of Fundamental and Interdisciplinary Sciences, Harbin Institute of Technology, Harbin 150080, China*

(Received 8 January 2018; published 20 April 2018)

Using a dynamic eigenresponse theory, we study the topological edge plasmon modes in dispersive plasmonic lattices constructed by unit cells of multiple nanoribbons. In dipole approximation, the bulk-edge correspondence in the lattices made of dimerized unit cell and one of its square-root daughter with nonsymmorphic symmetry are demonstrated. Calculations with consideration of dynamic long-range effects and retardation are compared to those given by nearest-neighbor approximations. It is shown that nonsymmorphic symmetry opens up two symmetric gaps where versatile topological edge plasmon modes are found. Unprecedented spectral shifts of the edge states with respect to the zero modes due to long-range coupling are found. The proposed ribbon structure is favorable to electrical gating and thus could serve as an on-chip platform for electrically controllable subwavelength edge states at optical wavelengths. Our eigenresponse approach provides a powerful tool for the radiative topological mode analysis in strongly coupled plasmonic lattices.

DOI: [10.1103/PhysRevB.97.144203](https://doi.org/10.1103/PhysRevB.97.144203)**I. INTRODUCTION**

Bulk-edge correspondence of crystals explained by topological band theory have been an area of intense study in condensed matter theory [1–4]. Recently, topological modes protected by various global or crystalline space group symmetries have attracted a lot of interest in the field of photonics because they could offer new opportunities in controlling light, such as robust transport of electromagnetic waves which are immune from backscattering due to disorder or defect [5–7]. Many interesting topological edge modes in periodic photonic systems with symmorphic symmetries have been designed and realized in the past few years [8–17].

The search for new confined topological photonic modes at higher frequencies is important for actual photonic applications due to the demand of high data rate and strong light-matter interaction. In the optical subwavelength region, it has been shown that topological edge states can be realized in one-dimensional (1D) biparticle chains [18–23], two-dimensional (2D) honeycomb lattices of plasmonic nanoparticles [24], and 2D plasmonic materials [25]. Owing to the ability of confining optical energy into the nanometer scale, topological plasmon modes provide a ubiquitous platform to enhance light-matter interaction in deep subwavelength volume.

Nonsymmorphic symmetry plays an important role in the prediction of new phases of matter, such as 2D Dirac semimetals [26] and symmetry-protected topological modes in three dimensions [14]. Recently, it is shown that new topological modes can be derived from taking nontrivial square roots for the tight binding Hamiltonian [27], which can lead to nonsymmorphic symmetry-protected topological modes. Realizations of these complex topological modes may require

more bulky designs due to more complex unit cells. Low dimensional plasmonic systems based on nanoribbons may offer opportunities to maintain these topological systems in the optical subwavelength regimes. In this paper, we study the radiative topological plasmon modes on plasmonic nanoribbon lattices protected by nonsymmorphic symmetry using the 2D version of eigenresponse theory [28]. The proposed nanoribbon array in three dimensions has a continuous translational symmetry along the y axis (see Fig. 1) and a discrete translational symmetry along the x axis. Since we only discuss the structure of the cross sections (as a 2D space in the xz plane), we will refer to the array as a 2D system. The ultrathin nanoribbon design supports plasmonic resonances in the visible and near infrared (vis-NIR) region, which could be favorable to fast dynamical tunability upon realistic electrical doping compared to the other geometries. Moreover, our eigenresponse theory provides spectral information for the band structure and edge states supported by the lattices with realistic effects such as the dynamic long-range interaction with retardation taken into account. For a comparison, we first calculate the band structures and the edge states of 1D biparticle lattices of both Su-Schrieffer-Heeger (SSH) [29] and Rice-Mele (RM) models [30,31]. Different from the other plasmonic geometries with multiple particles per unit cell [32,33], the SSH chain is the simplest model supporting the topological edge state. It is found that the edge state by including long-range coupling is blue-shifted from the zero mode predicted with only nearest-neighbor coupling. We further consider a nonsymmorphic extension of the RM lattice. The nonsymmorphic RM lattice can be obtained as the square root of the tight binding Hamiltonian of the parent RM lattice. Owing to the nonsymmorphic symmetry, two new gaps emerge symmetrically in the positive and negative bands of the parent lattice, which support multiple topological edge states [27]. Compared with the biparticle lattice, the edge states

*kin-hung.fung@polyu.edu.hk

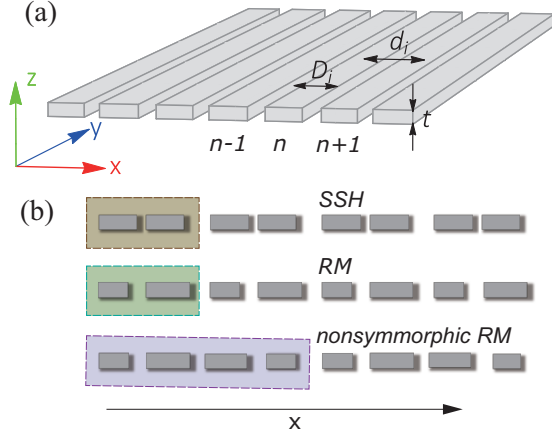


FIG. 1. (a) Schematic illustration of 1D array of nanoribbons. (b) Cross sections in the xz plane of SSH, RM, and nonsymmorphic extension of RM lattices. The thicknesses are enlarged for better illustration.

with long-range coupling in the nonsymmorphic, square rooted lattices can either blue-shift or keep invariant depending on the resident gaps. These results indicate the important role of long-range coupling on the spectral properties of the plasmonic arrays.

This paper is organized as follows. Section II devotes the general elements of the theory used in this work and in particular the dipolar response of the individual gold nanoribbon in the vis-NIR range and the eigenresponse theory in 2D space. The general results of this section are then applied in Sec. III, where the plasmonic band structure as well as the edge states of biparticle lattices, including both SSH and RM geometries are obtained. In Sec. IV, we discuss the band structure and the edge states in nonsymmorphic, square rooted lattices. Section V is devoted to discussions and conclusions.

II. THEORETICAL MODEL

A. LSP resonance of the individual nanoribbon

We begin by considering an array of thin metal nanoribbons located along the x axis as shown in Fig. 1(a). In the long wavelength limit in which a nanoribbon is close to its dipolar resonance, its near and far field responses are dominated by the electric dipole distribution. Within the dipole approximation, the n th effective dipole moment is related to the external applied electric field by $\mathbf{p}_n(\omega) = \alpha_n(\omega)\mathbf{E}_n(\omega)$ where $\alpha_n(\omega)$ is the dipolar polarizability tensor of the n th anisotropic particle. For the nanoribbon considered here whose thickness t is much smaller than the width D , the spectral location of the longitudinal dipolar resonance $\mathbf{p}_n \parallel \hat{\mathbf{x}}$ is far away from the transverse dipole $\mathbf{p}_n \parallel \hat{\mathbf{z}}$. If we restrict our attention on the x -polarization mode, it is reasonable to ignore the cross coupling from the z -component scattered fields by the other particles. In this case, the quasistatic longitudinal polarizability per unit length of the nanoribbon can be written as

$$\alpha(\omega) = \frac{D^2}{16} \frac{\varepsilon(\omega) - 1}{\varepsilon(\omega) + \chi}, \quad (1)$$

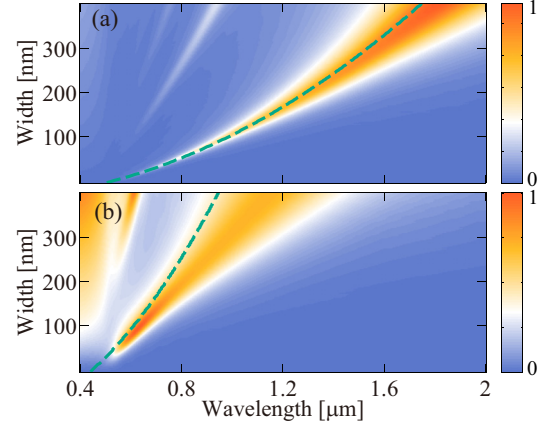


FIG. 2. Normalized extinction spectra of the individual Au nanoribbons with thickness. (a) $t = 2.4$ nm and (b) $t = 9.6$ nm for different widths. The dashed green line represents the dipolar resonant frequency calculated based on the polarizability Eq. (1).

where $\chi = D/t \gg 1$ is the aspect ratio, and $\varepsilon(\omega)$ is the relative permittivity of the metal. This expression is obtained from the infinite aspect ratio limit of the elliptical cylinder, and is similar to the expression of Ref. [34]. In the electrostatic case $\omega \rightarrow 0$ under normal incidence, the polarizability turns to be $\alpha_0 = D^2/16$ which is consistent with the perfect conductor limit of metal sheet [35]. We consider the nanoribbon of width D extracted from a single (111) atomic layer of gold [36]. By assuming the thickness of the gold monolayer is equal to a single (111) atomic layer $a_0 = 0.236$ nm, we choose the thickness of the nanoribbon to be $t = 2.4$ nm (about 10 atomic layers). For the dielectric property of the metal, we adopt the Drude model in order to obtain a semianalytical calculation:

$$\varepsilon(\omega) = \varepsilon_\infty - \frac{\omega_p^2}{\omega(\omega + i\tau^{-1})}, \quad (2)$$

where ε_∞ is the high frequency limit of the dielectric constant which accounts for background screening due to bound electrons, ω_p is the bulk plasma frequency, and τ^{-1} relates to the electron damping rate in the material. In the vis-NIR region, the following set of parameters is used to fit the experimental data for gold [37]: $\varepsilon_\infty = 9$, $\hbar\omega_p = 8.95$ eV, and $\hbar\tau^{-1} = 65.8$ meV.

From the dipolar polarizability $\alpha(\omega)$, the extinction cross section of the individual nanoribbon is given by $\sigma^{\text{ext}} = (8\pi^2/\lambda_0)\text{Im}\{\alpha\}$ [38]. Figures 2(a) and 2(b) show the dependence of the extinction cross section spectra σ^{ext} of the nanoribbon on the width D for $t = 2.4$ nm and 9.6 nm, respectively. The green dashed lines are calculated based on $\alpha(\omega)$. The density plots are numerically simulated with a full wave finite difference time domain (FDTD) solver Lumerical FDTD Solutions with x -polarized normal incidence. From the figure, we can find (1) the dipolar polarizability based on Eq. (1) for $t = 2.4$ nm is in good agreement with the lowest order dipole resonance from FDTD simulation. While for the thicker nanoribbon $t = 9.6$ nm, a blue-shift for the analytical calculation is observed especially for larger D . The discrepancy indicates that the influence of the nonvanishing thickness t for finite χ can't be ignored at the operating wavelengths. However, the quasistatic polarizability is accurate enough for

ultrathin nanoribbons considered here. (2) The dipolar plasmon wavelength increases monotonically with increasing width D , exhibiting an approximate $\propto \chi(=\sqrt{D/t})$ dependence [34]. A qualitative estimation can be established by neglecting the background screening ($\varepsilon_\infty = 1$), thereafter the polarizability can be simplified to

$$\alpha(\omega) \approx \frac{D^2}{16} \frac{\omega_p^2}{\omega_p^2 - \chi\omega(\omega + i\tau^{-1})}. \quad (3)$$

There appears a geometric resonant frequency $\omega_g = \chi^{-1/2}\omega_p$ in Eq. (3) which indicates the geometric dependence of the LSP. Owing to the geometric dependence, the resonant wavelength can be engineered by simply tailoring the ribbon's aspect ratio. As an example, the LSP resonance lies in the visible region for the nanoribbon $t = 2.4$ nm with width ranging from ~ 10 nm to 70 nm. Moreover, the bulk plasma frequency $\omega_p = \sqrt{ne^2/\varepsilon_0 m}$ for the nanoribbon can be effectively tuned by injecting charge carriers with conventional electric gating technology as in graphene nanostructures [39]. Thus electrically doped nanoribbons with a realistic doping level allow the LSP mode to be dynamically tuned across a broader spectral band, enabling potential applications for dynamic sensing and integrated on-chip information processing.

B. Eigenresponse theory in 2D space

A widely applied approach toward the topological eigenmode analysis is built on the coupled dipole method with quasistatic nearest-neighbor coupling. For example, plasmonic edge modes are analytically predicted at the zero mode frequencies associated with the single particle plasmon resonances in plasmonic SSH lattices [29] from both classical [18–22] or quantum [23] approaches. Unlike most electric systems, optical systems in general have inherent frequency dispersion together with radiative and absorption damping. Thus, it is highly desirable to develop an exactly solvable approach for the edge states in optical systems analysis with long-range coupling, especially for strongly coupled lattices of plasmonic or dielectric resonators.

In the following, we introduce the eigenresponse theory in 2D space with which we can calculate the plasmonic band structures as well as the edge states supported by the lattice. The eigenresponse theory is based on the coupled dipole method which has been applied for the optical properties of various plasmonic lattices. As previously shown, the nanoribbons in the lattices are well approximated as point dipoles in the long wave region. Hence, the local electric field at the position of a specific dipole inside the lattice is given by the external incident field and the fields produced by all the other dipoles. Dipole-dipole interaction among the particles leads to the following self-consistent coupled dipole equations [40–42]:

$$\mathbf{p}_n = \alpha_n \left(\mathbf{E}_n^{\text{ext}} + 4\pi k_0^2 \sum_{m \neq n} \mathbb{G}_{nm} \mathbf{p}_m \right), \quad (4)$$

where α_n is the polarizability of the n th ribbon, $\mathbf{E}_n^{\text{ext}}$ is the incident electric field at the n th dipole, the sum yields the electric field produced on site n by the rest of particles,

mediated by the 2D free space Green dyadics [43]:

$$\mathbb{G}_{nm} = \left(\mathbb{I} + \frac{1}{k_0^2} \nabla_\perp \nabla_\perp \right) g_0(k_0 \rho_{nm}). \quad (5)$$

Here \mathbb{I} is the 2×2 identity matrix, $k_0 = 2\pi/\lambda_0$ is the wave vector in vacuum, $\nabla_\perp = (\partial/\partial x, \partial/\partial z)$ is the 2D derivative operator, $\rho_{nm} = |\rho_n - \rho_m|$ is the interparticle spacing in the xz plane between sites n and m , and $g_0(k_0 \rho) = (i/4)H_0^{(1)}(k_0 \rho)$ denotes the 2D scalar Green function, where $H_0^{(1)}$ is the zero order Hankel function of the first kind. Because we are only interested in the longitudinal coupling, the Green dyadics becomes a scalar function $G(\rho) := (\mathbb{G})_{xx}(k_0 \rho) = (i/4k_0 \rho)H_1^{(1)}(k_0 \rho)$ where $H_1^{(1)}$ is the first-order Hankel function of the first kind. From the asymptotic expansion of $H_1^{(1)}$ along the x axis, we find that the dipole-dipole interaction in the quasistatic near field limit behaves as an inverse-square function of the distance,

$$G(\rho) = \frac{1}{2\pi k_0^2 \rho^2}, \quad (\rho \rightarrow 0). \quad (6)$$

Compared with the near field behavior of Green dyadics in three-dimensional (3D) space $\sim (k_0 r)^{-3}$, the near field of the dipole decays slowly in 2D space. In the coupled dipole theory, Eq. (4) can be rearranged to the eigenvalue problem,

$$\alpha_n^{-1} \mathbf{p}_n - 4\pi k_0^2 \sum_{m \neq n} \mathbb{G}_{nm} \mathbf{p}_m = \mathbf{E}_n^{\text{ext}}, \quad (7)$$

which relates the dipole moment distribution on the lattice with the external field. Here the polarization state is the eigenvector associated for the effective polarizability matrix $\mathbf{M}(\omega)$ [left side of Eq. (7)] with a specific driving field. However, all the spectral information of the system are contained in \mathbf{M} . In the eigenresponse theory, we consider the eigenvalue problem for the $\mathbf{M}(\omega)$ matrix without specifying the driving field by which we can obtain all the possible eigenmodes of a finite or infinite lattice. To be specific, we solve the algebraic eigenvalue problem [20,28],

$$\mathbf{M}(\omega) \mathbf{p} = \lambda(\omega) \mathbf{p}, \quad (8)$$

where \mathbf{M} is given by

$$[\mathbf{M}(\omega)]_{nm} = \begin{cases} \alpha_n^{-1}, & n = m; \\ -(i\pi k_0/\rho)H_1^{(1)}(k_0 \rho), & n \neq m, \end{cases}$$

and the eigenvector $\mathbf{p}(\omega) = [\mathbf{p}_1, \dots, \mathbf{p}_N]^T$ where N denotes the total particle number. So that the \mathbf{M} matrix can be regarded as the effective Hamiltonian for the plasmonic chain in which the diagonal term α_n^{-1} is analogous to the on-site energy for the n th particle, the off-diagonal Green functions are the hopping terms between the n th and m th sites. It should be noted that the effective Hamiltonian for the coupled optical system is inherently dispersive with loss, which makes it difficult to solve the eigenstates similar to the electronic counterpart.

For an infinite periodic lattice with M sites per unit cell, we seek the solution of the Bloch wave form $\mathbf{p}_n = \mathbf{p} e^{inka}$ with $k \in [-\pi/a, \pi/a]$ the Bloch wave vector. Inserting the Bloch ansatz into the coupled dipole equations (8) leads to the Bloch eigenvalue problem:

$$\mathbf{M}(\omega, k) \mathbf{p} = \lambda(\omega, k) \mathbf{p}, \quad (9)$$

where the elements of the M dimensional \mathbf{M} matrix in the \mathbf{p}_n basis are given by

$$[\mathbf{M}(\omega, k)]_{nm} = \begin{cases} \alpha_n^{-1} - \frac{i\pi k_0}{\rho} \sum_{p \neq 0} H_1^{(1)}(k_0 \rho) e^{ipka}, & n = m; \\ -\frac{i\pi k_0}{\rho} \sum_{p=-\infty}^{\infty} H_1^{(1)}(k_0 \rho) e^{ipka}. & n \neq m; \end{cases}$$

Here $\rho = |pa + d_{nm}|$ with d_{nm} is the spacing between the n th and m th particles in the unit cell and the eigenvector is $\mathbf{p} = [p_1, \dots, p_M]^T$ with M sites per unit cell.

From the \mathbf{M} matrix we can solve the complex eigenvalue $\lambda(\omega)$ for each ω in a finite lattice or (ω, k) in a periodic lattice. We note that $\lambda^{-1}(\omega)$, which contains all the spectral information of the collective eigenmodes, represents the inverse eigenpolarizability of the lattice [28]. Furthermore, the imaginary part $\text{Im}[\lambda^{-1}(\omega)]$ is proportional to the density states of the lattice and its peak gives rise to the eigenmode frequency and resonance width of the system.

C. General considerations

Let us have a look at the general features of the proposed nanoribbon lattices in the framework of the coupled dipole model where \mathbf{M} plays the same role as the Hamiltonian in the electronic system. In spite of the various analogies, optical systems are certainly significantly different from the condensed matter systems. In general, any optical material must include loss and dispersion to satisfy the causality principle. Consequently, one typically encounters decaying quasinormal modes related to a non-Hermitian algebraic eigenvalue problem with complex eigenvalues, that is, $\mathbf{M} \neq \mathbf{M}^\dagger$. In the coupled dipole approximation, the time reversal symmetry is broken because $\mathbf{M} \neq \mathbf{M}^*$ in the presence of material and radiation loss. However, it is usually believed that optical systems with weak damping still sustain the topological characteristics. Actually, the \mathbf{M} matrix considered in this work is symmetric by construction. This special feature leads to the observation of topological phases in several 1D and 2D lattices of dielectric [18] or plasmonic resonators [19–21, 23] with similar sublattice geometry as in their electronic counterparts. In addition, most optical resonant modes are featured with a finite band width which characterizes the mode's quality factor. This leads to the difficulty in spectrally resolving the exact band structure in plasmonic structures. In typically reported topological plasmonic systems mentioned above, the material and/or the radiation loss are neglected to obtain analytically real dispersion relations. Moreover, the material dispersion together with the long range dipole-dipole interaction gives rise to the asymmetry between the different bands protected by the global symmetries. In this work, however, we include both the material and radiation loss within the eigenresponse approach.

III. EDGE STATES IN BIPARTICLE LATTICES

A. Modal dispersion of biparticle lattices

In Sec. II, we have studied the spectral feature of the dipolar LSP mode of an isolated nanoribbon and introduced the eigenresponse theory in 2D space. In this section, we

apply the established method on the simple but instructive case of the arrays consisting of a biparticle lattice with two sites per unit cell. The biparticle lattice can mimic either the SSH model for polyacetylene which has been studied in topological photonics [9, 12, 13, 16, 20–23] or the RM model for conjugated diatomic polymers depending on the parameters. For a periodic lattice with two sites per unit cell, the \mathbf{M} matrix is given by

$$\mathbf{M}(\omega, k) = \begin{bmatrix} \alpha_1^{-1} - G_{AA} & -G_{AB} \\ -G_{BA} & \alpha_2^{-1} - G_{BB} \end{bmatrix}, \quad (10)$$

where $G_{AA} = G_{BB}$ and

$$G_{AA} = i\pi k_0 / \rho \sum_{p \neq 0} H_1^{(1)}(k_0 \rho) e^{ipka},$$

$$G_{AB} = \sum_{p \geq 0} (G_{d_A+pa} e^{ipka} + G_{d_B+pa} e^{-ik(p+1)a}),$$

$$G_{BA} = \sum_{p \geq 0} (G_{d_A+pa} e^{-ipka} + G_{d_B+pa} e^{ik(p+1)a}).$$

When the inverse on-site polarizabilities of the two sites are tuned to be equal ($\alpha_1^{-1} = \alpha_2^{-1}$), the above model describes the plasmonic analogy of the SSH chain [Fig. 1(b)]. In this case, it is known that the bulk \mathbf{M} exhibits two distinct topological phases for $d_1 < d_2$ and $d_1 > d_2$, separated by a topological transition point at $d_1 = d_2$. As a result, band inversion occurs across the transition point by which the Zak phase θ_{Zak} change from 0 to π . When the on-site polarizabilities are tuned to be different $\alpha_1^{-1} \neq \alpha_2^{-1}$, the system models the RM lattice which describes a linearly conjugated diatomic polymer; in this case, there is no inversion center in the unit cell and θ_{Zak} takes a fractional value, indicating no topological transition point corresponding to gap closure.

In order to gain analytical understanding similar to the standard tight binding model, we first consider the nearest neighboring coupling for Eq. (10). For the sake of simplicity, we introduce the parameters $\alpha_0^{-1} = (\alpha_1^{-1} + \alpha_2^{-1})/2$, $\Delta = (\alpha_1^{-1} - \alpha_2^{-1})/2$ and regard α_0^{-1} as a reference point (zero mode) for the eigenvalue problem. With these terms, \mathbf{M} reads

$$\mathbf{M}(\omega, k) = \begin{bmatrix} \Delta & -(t_1 + t_2 e^{-ika}) \\ -(t_1 + t_2 e^{ika}) & -\Delta \end{bmatrix}, \quad (11)$$

where $t_i = G_{d_i} = -(i\pi k_0 / d_i) H_1^{(1)}(k_0 d_i)$, ($i = 1, 2$). In Fig. 3, we have compared the polarizability difference Δ with the near field hopping interaction based on Eq. (6). Here, the staggered nanoribbons are chosen to be 50 and 60 nm in width. Obviously, the hopping term for distance larger than 50 nm is comparable with Δ , leading to the formation of the band gap structure which can be confirmed with the rigorous calculations. For the biparticle lattice considered here, the dispersion relation $\omega(k)$ can be explicitly solved. However, the analytical solutions are very difficult to find for complex geometries such as the lattice with four sites per unit cell considered in the next section. Since what is important is the critical condition for band inversion, we regard Δ , t_1 , and t_2 as independent parameters by which we yield the formal solution for $\lambda(\omega, k)$, giving rise to information on the band structure.

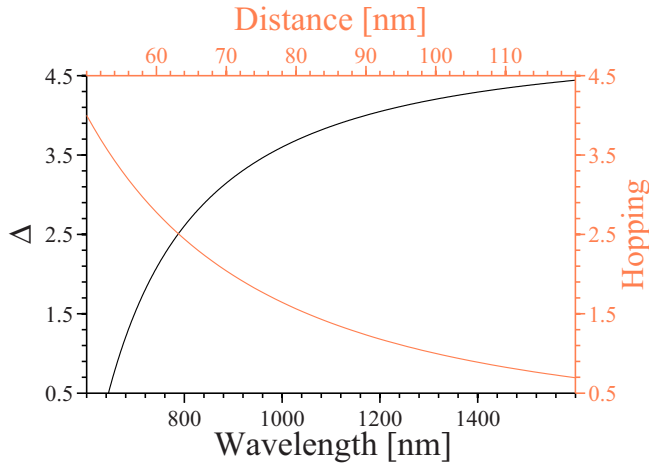


FIG. 3. Comparison between the on-site energy difference $\Delta(\rho)$ with the near field dipole-dipole hopping interaction.

Formally solving the eigenvalue problem, we obtain the following solutions for λ :

$$\lambda(\omega, k) = \pm \sqrt{\Delta^2 + t_1^2 + t_2^2 + 2t_1 t_2 \cos ka}. \quad (12)$$

As a result, there appears two symmetric bands which are separated by a frequency gap due to the staggered on-site polarizabilities and interparticle spacings. At the edge of the Brillouin zone $k = \pm \frac{\pi}{a}$ ($d = d_1 + d_2$), the gap width is given by

$$\Delta\lambda = 2\sqrt{\Delta^2 + (t_1 - t_2)^2} \geq 2|\Delta|. \quad (13)$$

The above band width becomes $\Delta\lambda = 2|t_1 - t_2|$ for the SSH lattice when $\Delta = 0$, which gives rise to the topological band inversion condition $t_1 = t_2$, i.e., $d_1 = d_2$, in the SSH lattice. In contrast, the parameter space (Δ, t_1, t_2) cannot be divided to disconnected patches by the line $\Delta = 0, t_1 = t_2$. As a result, the edge states in the RM lattice are not topological since they can be moved to the continuum continuously without having the gap closure.

Special attention is the spectral positions where $k = \pm\pi/a$ ($a = 2d$) for further reference. $k = \pm\pi/a$ define one-half of the first Brillouin zone of the dimered lattice, corresponding to the Brillouin zone with four sites per unit cell which is considered in the next section. In fact, we find $\lambda_{\pm\frac{\pi}{a}} = \pm\sqrt{\Delta^2 + t_1^2 + t_2^2}$ from Eq. (13), indicating that both bands are continuous at this k point.

Figure 4(a) presents the band structure for the SSH lattice by directly solving the eigenvalue for the matrix given in Eq. (10). The geometric parameters are shown in Table I. In the figure, we plot $\text{Max}[\text{Im}(\lambda^{-1}(\omega, k))]$ for each (ω, k) pair in the vis-NIR region. To make a comparison with the nonsymmorphic RM lattice with four sites per unit cell [shown in Fig. 1(b)], we have used the composite unit cell with four sites for the biparticle lattices. As a result, there appears four branches in each geometry where the centered two branches are folded from the original larger Brillouin zone. The left and right parts of the band structure correspond to the nearest neighbor and long-range coupling calculations, respectively. From the nearest-neighbor calculations, it is found that the

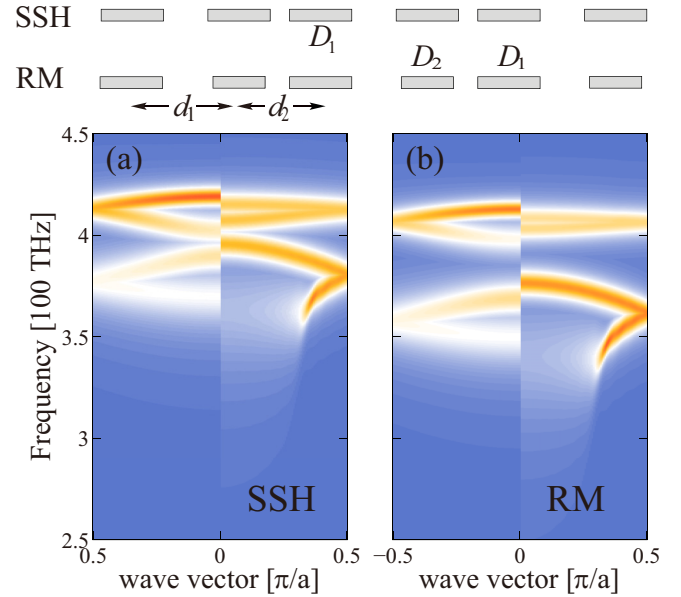


FIG. 4. Band structures for (a) SSH lattice and (b) RM lattice. To compare the band structures for the extended nonsymmorphic lattices, we choose four nanoribbons per unit cell in all the geometries. In both figures, the left part for $k \in [-0.5, 0]$ and the right part for $k \in [0, 0.5]$ correspond to the nearest neighboring and full coupling calculations, respectively.

two bands are symmetric with respect to the single particle resonant frequency which is consistent with the above formal analysis. However, the low frequency bright band is weaker and broader than the high frequency dark band. The relative weakness and broadness arises from the symmetric nature of the bright mode: The electronic dipoles in the two ribbons per unit cell are aligned along the same direction and decrease the dipolar restoring force associated with the lower band. At the same time, the bright modes are strongly coupled to radiation, especially for the lower part below the light cone. On the contrary, the dipole moments in the high frequency dark band are in opposite directions in the same unit cell which are weakly coupled to radiation and increase the restoring force, leading to an increase in the frequency compared with a single ribbon.

For the band structures with long-range coupling, a strong asymmetry between the bands is found for both the SSH and RM lattices: The high frequency band becomes narrower while the low frequency band is broadened when long-range coupling is accounted; as a result, the gap width decreases and shifts

TABLE I. Geometric parameters corresponding to the representative lattices of dimers (SSH and RM) and nonsymmorphic dimers whose band structures are shown in Figs. 4 and 8.

Geometric parameters	D_1 (nm)	D_2 (nm)	d_1 (nm)	d_2 (nm)
SSH	50	50	80	60
RM	50	60	80	60
Nonsymmorphic RM I	50	60	60	80
Nonsymmorphic RM II	50	55	70	60

towards high frequency globally. In the next section, we will discuss the consequence of the blue-shift of the gap on the spectral location of the edge state in the biparticle lattice. To explain the band gap behaviors with long-range coupling, it is useful to consider the dipole distributions for modes near the band edges. For modes near the upper band edge of the high frequency band, the dipole distributions in adjacent unit cells are aligned with the reference unit cell, which decrease the dipolar restoring force, thus leading to a lower frequency. In contrast, the dipole moments in the adjacent unit cell at frequency near the lower band edge of the dark band are opposite the dipoles in the reference unit cell, which leads to blue-shift towards higher frequency. A similar argument can explain the reversal behavior for the low frequency band with long-range coupling when the opposite dipole moments in the unit cells are noticed.

B. Edge states in biparticle lattices

It is known that the truncated 1D lattice supports the edge state on its boundary. In the nearest-neighbor coupling model of the SSH lattices, these edge states correspond to the zero modes of the systems. To better understand the edge states in our system, we first consider a semifinite chain with one boundary following Ref. [13]. The edge state can be solved from the coupled equations:

$$\begin{aligned} -t_2 d_{n-1} + \Delta c_n - t_1 d_n &= \lambda c_n, \\ -t_1 c_n - \Delta d_n - t_2 c_{n+1} &= \lambda d_n, \end{aligned}$$

where c_n, d_n are the dipole amplitudes at each site in the n th unit cell. For the edge state which exponentially decays along the lattice, we consider the following solutions: $c_n = c(-1)^n e^{-\kappa n a}$, $d_n = d(-1)^n e^{-\kappa n a}$. Inserting the decaying solution into the above coupled equations, we find the dipole amplitude ratio is given by

$$\frac{c}{d} = \frac{\Delta \pm \sqrt{\Delta^2 + (t_2 e^{-\kappa a} - t_1)(t_2 e^{\kappa a} - t_1)}}{t_2 e^{-\kappa a} - t_1}, \quad (14)$$

associated with eigenvalues,

$$\begin{aligned} \lambda &= \pm \sqrt{\Delta^2 + (t_2 e^{-\kappa a} - t_1)(t_2 e^{\kappa a} - t_1)} \\ &= \pm \sqrt{\Delta^2 + t_1^2 + t_2^2 - 2t_1 t_2 \cosh \kappa a}, \end{aligned} \quad (15)$$

where the positive and negative eigenvalue solutions have a positive and a negative amplitude ratio, respectively. The decay constant κ must lie in the range $0 \leq \kappa \leq \kappa_c$ where $\kappa_c = \ln(t_2/t_1)/a$. Special attention is the SSH model with $\Delta = 0$. In this case $\kappa = \kappa_c$ is the mid-gap solution of the zero eigenvalue, while the solution $\kappa = 0$ corresponds to the band edge state.

We now consider the semi-infinite long lattice where the first site is particle A with hopping t_1 . Then the lattice can be described by the following coupled equations:

$$\begin{aligned} \Delta c_n - t_1 d_n - t_2 d_{n-1} &= \lambda c_n, & \text{for } n \geq 2 \\ -\Delta d_n - t_1 c_n - t_2 c_{n+1} &= \lambda d_n, & \text{for } n \geq 1, \end{aligned} \quad (16)$$

together with the boundary condition,

$$\Delta c_1 - t_1 d_1 = \lambda c_1.$$

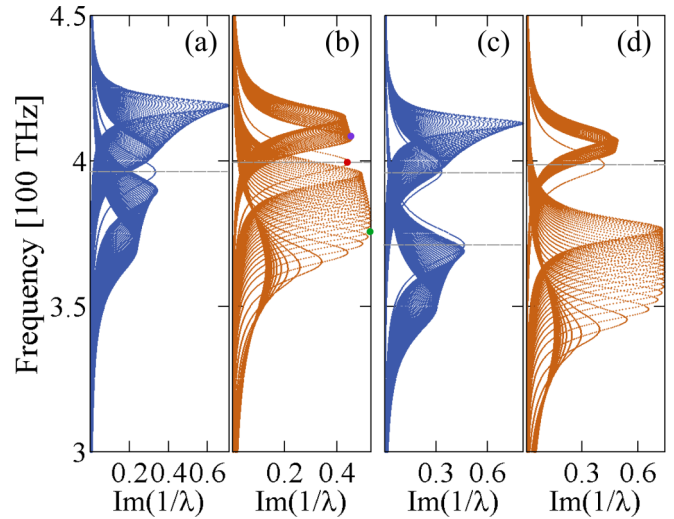


FIG. 5. Band structures of finite lattices of the SSH model [(a) and (b)] with 81 sites, and the RM model [(c) and (d)] with 82 sites. Here, (a) and (c) and (b) and (d) are based on nearest-neighbor and long-range coupling calculations, respectively.

The solution of the coupled equation which satisfied with the above boundary condition is

$$\lambda = \Delta, \quad (17)$$

with the eigenstates of the following form:

$$c_n = \alpha(-1)^n \left(\frac{t_1}{t_2}\right)^n, \quad d_n = 0. \quad (18)$$

The decaying solution for the edge state from the above equation is finite as $n \rightarrow +\infty$ if $t_1 < t_2$. This solution becomes the zero mode in the SSH model for $\Delta = 0$.

The above analysis provides a qualitative estimate for the edge state in our system. Figures 5(a) and 5(b) present the band structure for a finite SSH lattice with odd number $N = 81$ nanoribbons by nearest-neighbor and long-range coupling calculations, respectively. For each frequency, we plot the imaginary parts of λ^{-1} . Because there are odd number particles, the two boundaries of the lattice correspond to two different bulk phases with $t_1 > t_2$ and $t_1 < t_2$. Therefore, a topological edge state exists on the boundary with $t_1 < t_2$ with a zero mode frequency as pointed out by the above analysis. This can be verified by Fig. 5(a), where the edge state lies in the center of the gap for the nearest neighboring coupling. However, Fig. 5(b) indicates that the edge state shifts towards higher frequency when long-range coupling is included. The blue-shift of the topological edge state in the SSH model is a consequence of the blue-shift of the gap. As is pointed out earlier, the observed spectral shifts due to long-range coupling origins from the symmetry of the dipole moments in the nearby unit cell. This is verified by Fig. 6 where the long-range coupling increases the restoring force for the edge state and lower band. For comparison, we show in Fig. 5(c) the band structure for a finite 82 RM lattice with nearest-neighbor coupling. As predicted by the analysis Eq. (16), there are two nontopological edge states lying at the respective single particle resonances. It is very interesting to note that in Fig. 5(d) the lower edge state

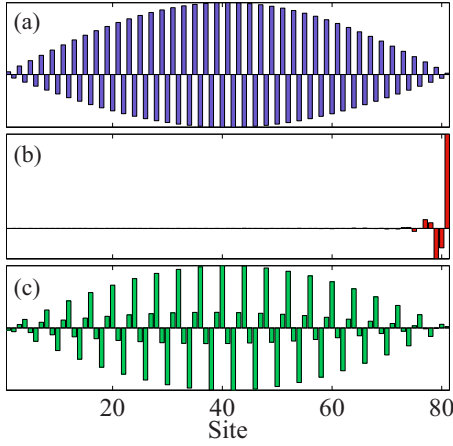


FIG. 6. Dipole moment distributions for states in (a) the upper band, (c) lower band, and (b) the edge state corresponding to the band structure in Fig. 5(b).

merges into the low frequency band when long-range coupling is included.

In Fig. 7, we show the spectral shift of the corresponding edge states with respect to the single particle resonance, using the long-range coupling calculations for both SSH and RM lattices. Here, d_1 is fixed to 50 nm while d_2 changes from 70 nm to 130 nm. It is found that the spectral shift decreases monotonically when d_2 increases in both lattices. This behavior is in agreement with the above analysis for band structure based on coupling strength.

IV. NONSYMMORPHIC RM LATTICES

A. Modal dispersion of nonsymmorphic RM lattices

In Sec. III, we have studied the band structures for arrays consisting of biparticle lattices and revealed the unexpected blue-shift of the edge mode. Here we consider the nonsymmorphic extension of the plasmonic RM lattice with full dispersion and loss, which has the same lattice geometry as the coupled waveguide system in [27]. The nonsymmorphic symmetry is a combination of point group operations with nonprimitive lattice translations acting on the unit cell of the parent lattice. Typical operations including glide or screw rotation with

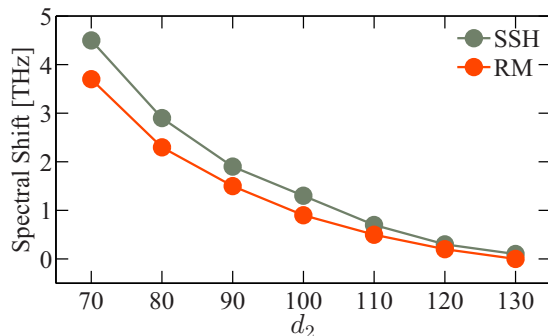


FIG. 7. Spectral shift of the edge state with respect to the single particle resonance for SSH and RM lattices. Here, we fix the interparticle spacing $d_1 = 60$ nm and vary d_2 from 70 to 130 nm.

fractional lattice translation. In electronic systems, it has been shown that the presence of nonsymmorphic symmetry leads to new topological phases which can be insulating [44,45] or semimetallic with Dirac points protected by nonsymmorphic symmetry [26,46]. Here, we apply nonsymmorphic symmetry to the RM lattice. To realize nonsymmorphic symmetry, we exchange the nanoribbons in the odd number unit cells while keeping the interparticle spacings invariant. Thus the nanoribbon widths in a unit cell are $D_1, D_2, D_2,$ and D_1 with a spatial inversion center which is absent in the RM lattice, indicating a one-half fractional lattice translation. We find that the nonsymmorphic symmetry opens new gaps for both the higher and lower frequency bands of the corresponding RM lattice.

As in the biparticle lattice, we first consider nearest-neighbor coupling in order to gain an intuitive picture for the overall band structure. For the nonsymmorphic lattice, the corresponding \mathbf{M} matrix is given by

$$\mathbf{M}(\omega, k) = \begin{pmatrix} \Delta & -t_1 & 0 & -t_2 e^{-ika} \\ -t_1 & -\Delta & -t_2 & 0 \\ 0 & -t_2 & -\Delta & -t_1 \\ -t_2 e^{ika} & 0 & -t_1 & \Delta \end{pmatrix}. \quad (19)$$

Here $\Delta, t_1,$ and t_2 are the same as in the previous section. We note that the \mathbf{M} matrix is equivalent to the tight binding Hamiltonian in Ref. [27]. In the following, we will revisit some key results of [27] including the symmetric bands as well as Zak phases which are indispensable for the analysis of the full model with dispersion, loss, and long-range coupling. Solving the eigenvalue problem for the \mathbf{M} matrix, we yield the formal solutions of the eigenvalue,

$$\lambda(\omega, k) = \pm \sqrt{\Delta^2 + t_1^2 + t_2^2 \pm 2t_1 \sqrt{\Delta^2 + t_2^2} \cos^2 \frac{ka}{2}}. \quad (20)$$

This leads to four symmetric bands with two positive and two negative eigenvalues. The two inner bands are given by

$$\sqrt{\Delta^2 + t_2^2} - t_1 < |\lambda| < \sqrt{(\Delta - t_1)^2 + t_2^2},$$

which are separated by an inner gap,

$$-\left(\sqrt{\Delta^2 + t_2^2} - t_1\right) < |\lambda| < \sqrt{\Delta^2 + t_2^2} - t_1. \quad (21)$$

Similarly, there are two outer bands,

$$\sqrt{(\Delta + t_1)^2 + t_2^2} < |\lambda| < \sqrt{\Delta^2 + t_2^2} + t_1.$$

The outer bands are separated from the inner bands with two symmetric outer gaps,

$$\sqrt{(\Delta - t_1)^2 + \beta^2} < |\lambda| < \sqrt{(\Delta + t_1)^2 + t_2^2}. \quad (22)$$

Accordingly, the band edges are given by

$$E_{\pm} = \sqrt{\Delta^2 + t_2^2} \pm t_1^2, \quad \text{inner edges};$$

$$E'_{\pm} = \sqrt{(\Delta \pm t_1^2)^2 + t_2^2}, \quad \text{outer edges}.$$

Here, we emphasize again that the above solutions are based on a purely formal analysis. All the lattice parameters Δ, t_1, t_2 are complex functions of ω and the eigenvalue $\lambda(\omega, k)$ is a complex function of (ω, k) . The dispersion relation $\omega(k)$ could

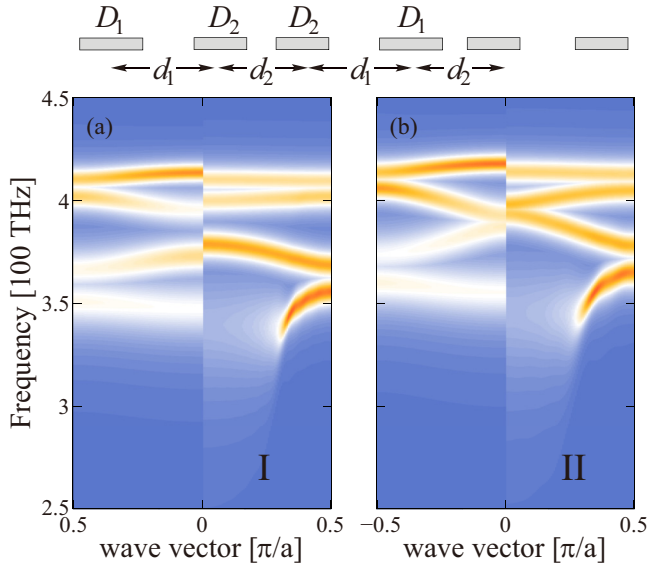


FIG. 8. Band structures for two representative nonsymmorphic biparticle lattices hosting edge states in different gaps. The geometric parameters are shown in Table I.

only be found by further calculation based on the above formal solutions. However, we are interested in the conditions for band inversion from which we can identify different topological phases with the same band structure as in the SSH model. In this respect, all the lattice parameters can be regarded as independent parameters which determine the final band structure.

To verify the above analysis based on nearest-neighbor calculations, Figs. 8(a) and 8(b) present the band structures for two representative lattices. The corresponding geometric parameters are given in box I. As previously, the left and right parts in Figs. 8(a) and 8(b) are based on nearest-neighbor coupling and long-range coupling, respectively. It is found that the four bands are paired symmetric for the nearest-neighbor coupling case, which is in agreement with the above formal analysis. In Fig. 8(a), the lattice constants are the same as in Fig. 4, and the corresponding locations of bands are very similar to each other despite the opening of two symmetric outer gaps at the edge of the Brillouin zone. Thus, the nonsymmorphic symmetry gives rise to the emergent gaps. Another feature for the nonsymmorphic lattice is that the two positive frequency bands become narrower while the two negative bands become broader when long-range coupling is considered. As a result, the width of the central gap decreases and shifts towards higher frequency similar to the biparticle lattice; the two new outer gaps become narrower while keeping the gap centers invariant. A similar band structure is also found for another set of parameters shown in Fig. 8(b). Besides the similarities, we should point out that the central gap in the nonsymmorphic lattice vanishes if $t_1 = \sqrt{\Delta^2 + t_2^2}$, which is different from the case of the RM lattice where the gap never closes.

B. Edge states in nonsymmorphic RM lattices

We now consider the edge states in the nonsymmorphic RM lattices. Similar in the SSH model, both the inner and outer gaps' widths can vanish by tuning the lattice parameters.

TABLE II. Numerical calculated Zak phases for nonsymmorphic lattices I and II.

θ_{Zak}	Band 1	Band 2	Band 3	Band 4
Nonsymmorphic I	0	0	$-\pi$	$-\pi$
Nonsymmorphic II	0	π	0	$-\pi$

Thus we can define the following indices that characterize the band inversion condition for the gaps. For the central gap, the critical point for gap closure is $t_1 = \sqrt{\Delta^2 + t_2^2}$, by which we can define

$$\xi = \text{sgn}[\Delta^2 + t_2^2 - t_1^2]. \quad (23)$$

This means band inversion for the central gap occurs when ξ changes sign. For the outer gaps, the band inversion occurs when Δ changes its sign as in the SSH model, leading to another index,

$$\zeta = \text{sgn}[\Delta]. \quad (24)$$

The reason for introducing these indices is that the band inversion from the sign change of the indices gives rise to the same band structure but they belong to different topological phases, which is completely analogous to the topological analysis for the SSH model. The band inversion is an indication of topological phase. In the following we will demonstrate the existence of edge states in the gaps with the help of these topological indices (ξ, ζ) . In fact, the topological indices for band structures shown in Figs. 8(a) and 8(b) are $(\xi, \zeta) = (+, \pm)$ and $(-, \pm)$. Here it is understood that exchanging the values of D_1 and D_2 gives rise to the same band structure with opposite ζ .

We can verify the topological classification of these bands, by calculating the Zak phase for each band,

$$\theta_{\text{Zak}} = i \oint_{\text{BZ}} \langle \mathbf{p} | \frac{d}{dk} | \mathbf{p} \rangle dk. \quad (25)$$

The index $Z = \theta_{\text{Zak}}/\pi$ takes the integer number for a topological phase while it takes any value for nontopological phases. To compute θ_k numerically, we adopt the following discrete form:

$$\theta_{\text{Zak}} = \text{Arg} \left(\prod_i \frac{\langle \mathbf{p}_{i+1} | \mathbf{p}_i \rangle}{|\langle \mathbf{p}_{i+1} | \mathbf{p}_i \rangle|} \right), \quad (26)$$

where $\mathbf{p}_i = \mathbf{p}(k_i)$, $k_i \in [-\pi/a, \pi/a]$. For lattices with parameters given in Table I, θ_{Zak} associated with each band are given in Table II. From the table, θ_{Zak} for each band take the value either 0 or $\pm\pi$, indicating that the nonsymmorphic RM lattice belongs to topological phases. Meanwhile, all the Zak phases change signs when the sign of Δ changes, thereby supporting edge states in the gaps.

In Fig. 9, we present the band structure for a finite lattice containing $N = 82$ particles with long-range coupling. There appears an edge state in each of the outer gaps which are denoted with red and green dots. The corresponding state vectors are shown in Figs. 9(c) and 9(d). It is found the two edge states reside on the opposite boundaries, indicating opposite signs for Δ . Hence, they are resulted from the band inversion relating to the outer gaps with opposite ζ . Comparison with the nearest-neighbor coupling calculation, there is no obvious spectral shift

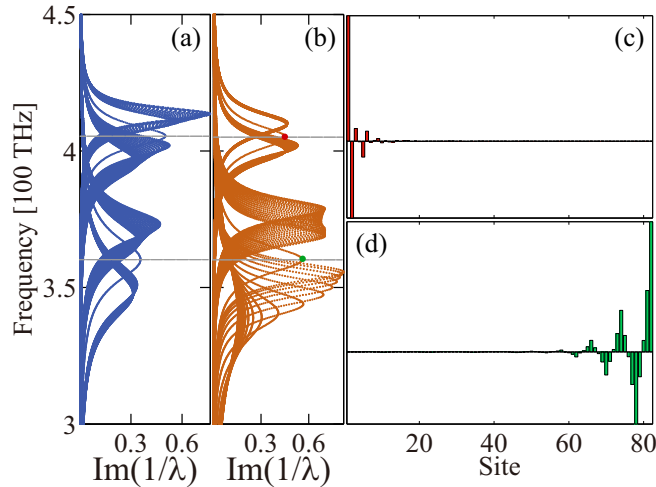


FIG. 9. (a) and (b) The band structure of the nonsymmorphic RM lattice with indices $(\xi, \zeta) = (+, \pm)$, where the colored dots denote the spectral position of the edge states. (c) and (d) The polarization state vectors for the two edge states.

for the edge states in the outer gaps when long-range coupling is included. This is different from the blue-shift of the edge state in the SSH lattice.

Figure 10 shows the band structure for another finite lattice with $N = 82$ particles whose bulk band structure is shown in Fig. 8(b). Comparing with lattice II shown in Fig. 9, there are an edge state in both the central and outer gaps, and two modes in the center gap. The eigenvectors for each edge state are depicted in Figs. 10(c)–10(f). It is shown that the two higher frequency modes reside on the left boundary while the lower two modes are supported by the right boundary. As in Fig. 9, we ascribe the two outer edge states to the band inversion from the sign change of ζ , while the two inner edge states come from the band inversion due to the sign change of ξ which controls the central gap. It is interesting to note that, similar to the case with $\zeta = +1$, the edge states in outer gaps don't show obvious spectral shift when long-range coupling is considered. In contrast, the edge states in the inner gap shift towards higher frequencies largely with long-range coupling.

V. CONCLUSION

In summary, we have used the eigenresponse theory to study the radiative topological edge plasmon modes in dispersive arrays constructed by unit cells of multiple nanoribbons. The bulk-edge correspondence for both dimerized unit cell and one of its square-root daughter with nonsymmorphic symmetry

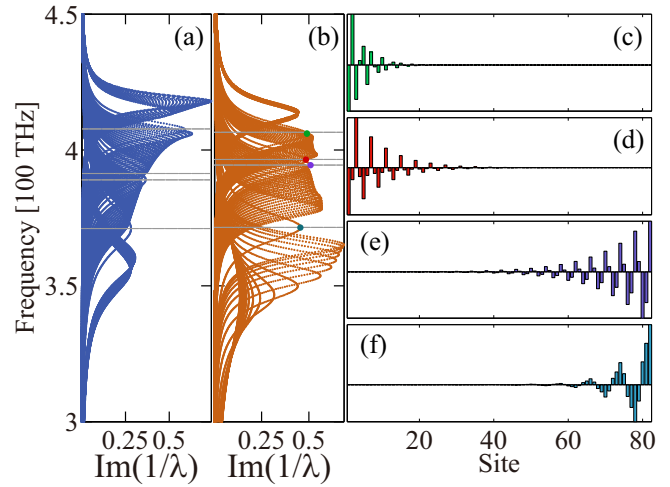


FIG. 10. (a) and (b) The band structure of the nonsymmorphic RM lattice with indices $(\xi, \zeta) = (-, \pm)$, where the colored dots denote the spectral position of the edge states. (c)–(f) The polarization state vectors for the four edge states denoted in (b).

are studied with most realistic effects including the material dispersion, absorption, retardation, and long-range coupling being considered. The resonant frequency of the edge state in the SSH model is blue-shifted from the theoretical prediction of zero mode based on the nearest-neighboring approximation. For the nonsymmorphic, square-root biparticle lattices, we demonstrate that new gaps arise symmetrically in the presence of the nonsymmorphic symmetry in which topological edge states in different gaps exhibit different responses for the long-range coupling. Our results clarify the crucial role of long-range coupling on the real modal properties of the topological plasmonic lattices. We believe that due to the simplicity and strength of our approach, it offers a powerful paradigm for the design and calculation of subwavelength topological phases at optical frequencies. Moreover, the suggested nanoribbon geometry could serve as an electronically tunable platform to enhance light-matter interaction in nanoscale for integrated on-chip applications.

ACKNOWLEDGMENTS

We thank Kai Guo, Cheng Qian, Wen Yan Wang, Kai Fung Lee, and Wang Tat Yau for illuminating discussions. This work was supported by Hong Kong Research Grant Council (Grants No. 15300315 and No. 15301917) and the Hong Kong Polytechnic University (Grants No. G-UC70, No. G-YBPT, and No. 1-ZVGH).

- [1] M. Z. Hasan and C. L. Kane, Topological insulators, *Rev. Mod. Phys.* **82**, 3045 (2010).
- [2] X. L. Qi and S. C. Zhang, Topological insulators and superconductors, *Rev. Mod. Phys.* **83**, 1057 (2011).
- [3] C. K. Chiu, J. C. Y. Teo, A. P. Schnyder, and S. Ryu, Classification of topological quantum matter with symmetries, *Rev. Mod. Phys.* **88**, 035005 (2016).

- [4] L. Fu, Topological Crystalline Insulators, *Phys. Rev. Lett.* **106**, 106802 (2011).
- [5] L. Lu, J. D. Joannopoulos, and M. Soljacic, Topological photonics, *Nat. Photon.* **8**, 821 (2014).
- [6] S. Raghu and F. D. M. Haldane, Analogs of quantum Hall effect edge states in photonic crystals, *Phys. Rev. A* **78**, 033834 (2008).

- [7] Z. Wang, Y. D. Chong, J. D. Joannopoulos, and M. Soljacic, Observation of unidirectional backscattering-immune topological electromagnetic states, *Nature (London)* **461**, 772 (2009).
- [8] M. C. Rechtsman, J. M. Zeuner, Y. Plotnik, Y. Lumer, D. Podolsky, F. Dreisow, S. Nolte, M. Segev, and A. Szameit, Photonic Floquet topological insulators, *Nature (London)* **496**, 196 (2013).
- [9] A. Blanco-Redondo, I. Andonegui, M. J. Collins, G. Harari, Y. Lumer, M. C. Rechtsman, B. J. Eggleton, and M. Segev, Topological Optical Waveguiding in Silicon and the Transition Between Topological and Trivial Defect States, *Phys. Rev. Lett.* **116**, 163901 (2016).
- [10] A. B. Khanikaev, S. H. Mousavi, W. K. Tse, M. Kargarian, A. H. MacDonald, and G. W. Shvets, Photonic topological insulators, *Nat. Mater.* **12**, 233 (2013).
- [11] M. Xiao, Z. Q. Zhang, and C. T. Chan, Surface Impedance and Bulk Band Geometric Phases in One-Dimensional Systems, *Phys. Rev. X* **4**, 021017 (2014).
- [12] K. H. Choi, C. W. Ling, K. F. Lee, Y. H. Tsang, and K. H. Fung, Simultaneous multi-frequency topological edge modes between one-dimensional photonic crystals, *Opt. Lett.* **41**, 1644 (2016).
- [13] T. J. Atherton, C. A. M. Butler, M. C. Taylor, I. R. Hooper, A. P. Hibbins, J. R. Sambles, and H. Mathur, Topological modes in one-dimensional solids and photonic crystals, *Phys. Rev. B* **93**, 125106 (2016).
- [14] L. Lu, C. Fang, L. Fu, S. G. Johnson, J. D. Joannopoulos, and M. Soljacic, Symmetry-protected topological photonic crystal in three dimensions, *Nat. Phys.* **12**, 337 (2016).
- [15] M. Hafezi, S. Mittal, J. Fan, A. Migdall, and J. M. Taylor, Imaging topological edge states in silicon photonics, *Nat. Photon.* **7**, 1001 (2013).
- [16] C. Poli, M. Bellec, U. Kuhl, F. Mortessagne, and H. Schomerus, Selective enhancement of topologically induced interface states in a dielectric resonator chain, *Nat. Commun.* **6**, 6710 (2015).
- [17] A. P. Slobozhanyuk, A. N. Poddubny, A. E. Miroshnichenko, P. A. Belov, and Y. S. Kivshar, Subwavelength Topological Edge States in Optically Resonant Dielectric Structures, *Phys. Rev. Lett.* **114**, 123901 (2015).
- [18] A. Poddubny, A. Miroshnichenko, A. Slobozhanyuk, and Y. Kivshar, Topological Majorana states in zigzag chains of plasmonic nanoparticles, *ACS Photon.* **1**, 101 (2014).
- [19] I. S. Sinev, I. S. Mukhin, A. P. Slobozhanyuk, A. N. Poddubny, A. E. Miroshnichenko, A. K. Samusev, and Y. S. Kivshar, Mapping plasmonic topological states at the nanoscale, *Nanoscale* **7**, 11904 (2015).
- [20] C. W. Ling, M. Xiao, C. T. Chan, S. F. Yu, and K. H. Fung, Plasmonic topological edge plasmon modes between diatomic chains of plasmonic nanoparticles, *Opt. Express* **23**, 2021 (2015).
- [21] C. X. Liu, M. V. Gurudev, and D. Pekker, Robust manipulation of light using topologically protected plasmonic modes, [arXiv:1610.8941](https://arxiv.org/abs/1610.8941).
- [22] D. E. Gomez, Y. Hwang, J. Lin, T. J. Davis, and A. Roberts, Plasmonic edge states: An electrostatic eigenmode description, *ACS Photon.* **4**, 1607 (2017).
- [23] C. A. Downing and G. Weick, Topological collective plasmons in bipartite chains of metallic nanoparticles, *Phys. Rev. B* **95**, 125426 (2017).
- [24] L. Wang, R. Y. Zhang, M. Xiao, D. Z. Han, C. T. Chan, and W. J. Wen, The existence of topological edge states in honeycomb plasmonic lattices, *New J. Phys.* **18**, 103029 (2016).
- [25] D. Jin, T. Christensen, M. Soljacic, N. X. Fang, L. Lu, and X. Zhang, Infrared Topological Plasmons in Graphene, *Phys. Rev. Lett.* **118**, 245301 (2017).
- [26] S. M. Young and C. L. Kane, Dirac Semimetals in Two Dimensions, *Phys. Rev. Lett.* **115**, 126803 (2015).
- [27] J. Arkininstall, M. H. Teimourpour, L. Feng, R. El-Ganainy, and H. Schomerus, Topological tight-binding models from non-trivial square roots, *Phys. Rev. B* **95**, 165109 (2017).
- [28] K. H. Fung and C. T. Chan, Plasmonic modes in periodic metal nanoparticle chains: A direct dynamic eigenmode analysis, *Opt. Lett.* **32**, 973 (2007).
- [29] W. P. Su, J. R. Schrieffer, and A. J. Heeger, Solitons in Polyacetylene, *Phys. Rev. Lett.* **42**, 1698 (1979).
- [30] M. J. Rice and E. J. Mele, Elementary Excitations of a Linearly Conjugated Diatomic Polymer, *Phys. Rev. Lett.* **49**, 1455 (1982).
- [31] M. Atala, M. Aidelsburger, J. T. Barreiro, D. Abanin, T. Kitagawa, E. Demler, and I. Bloch, Direct measurement of the Zak phase in topological Bloch bands, *Nat. Phys.* **9**, 795 (2013).
- [32] A. D. Humphrey and W. L. Barnes, Plasmonic surface lattice resonances in arrays of metallic nanoparticle dimers, *J. Opt.* **18**, 035005 (2016).
- [33] S. Baur, S. Sanders, and A. Manjavacas, Hybridization of lattice resonances, *ACS Nano* **12**, 1618 (2018).
- [34] F. J. Garcia de Abajo and A. Manjavacas, Plasmonics in atomically thin materials, *Faraday Discuss.* **178**, 87 (2015).
- [35] H. C. van de Hulst, *Light Scattering by Small Particles* (Dover, New York, 1981).
- [36] A. Green and E. Bauer, Gold monolayers on silicon single crystal surface, *Surf. Sci.* **103**, L127 (1981).
- [37] P. B. Johnson and R. W. Christy, Optical constants of the noble metals, *Phys. Rev. B* **6**, 4370 (1972).
- [38] F. J. Garcia de Abajo, Graphene plasmonics: Challenges and opportunities, *ACS Photon.* **1**, 135 (2014).
- [39] A. Manjavacas and F. J. Garcia de Abajo, Tunable plasmons in atomically thin gold nanodisks, *Nat. Commun.* **5**, 3548 (2014).
- [40] D. S. Citrin, Coherent excitation transport in metal-nanoparticle chains, *Nano Lett.* **4**, 1561 (2004).
- [41] V. A. Markel, Coupled-dipole approach to scattering of light from a one dimensional periodic dipole structure, *J. Mod. Opt.* **40**, 2281 (1993).
- [42] M. B. Ross, C. A. Mirkin, and G. C. Schatz, Optical properties of one-, two- and three-dimensional arrays of plasmonic nanostructures, *J. Phys. Chem. C* **120**, 816 (2016).
- [43] O. J. F. Martin and N. B. Piller, Electromagnetic scattering in polarizable background, *Phys. Rev. E* **58**, 3909 (1998).
- [44] C. X. Liu, R. X. Zhang, and B. K. VanLeeuwen, Topological nonsymmorphic crystalline insulators, *Phys. Rev. B* **90**, 085304 (2014).
- [45] K. Shiozaki, M. Sato, and K. Gomi, Topology of nonsymmorphic crystalline insulators and superconductors, *Phys. Rev. B* **93**, 195413 (2016).
- [46] Y. X. Zhao and A. P. Schnyder, Nonsymmorphic symmetry-required band crossings in topological semimetals, *Phys. Rev. B* **94**, 195109 (2016).